Heliyon 10 (2024) e31241

Contents lists available at ScienceDirect

Heliyon

journal homepage: www.cell.com/heliyon

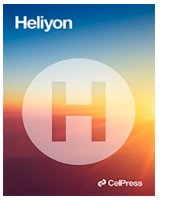

Research article

Quasi-10-day waves in temperature and polar mesospheric clouds: Results of AIM/SOFIE and Aura/MLS observations

Yucheng Su [a,1], Boyang Jiao [b,1], Shuai Fu [c,d,*], Yi Jiang [c,d,**]

[a] Zhuhai Public Meteorological Service Center, Zhuhai, 519000, People's Republic of China
[b] School of Atmospheric Sciences and Key Laboratory of Tropical Atmosphere-Ocean System, Ministry of Education, Sun Yat-sen University, Zhuhai, 519082, People's Republic of China
[c] State Key Laboratory of Lunar and Planetary Sciences, Macau University of Science and Technology, Taipa, 999078, Macau, People's Republic of China
[d] CNSA Macau Center for Space Exploration and Science, Taipa, 999078, Macau, People's Republic of China

ARTICLE INFO

Keywords:
Planetary waves
Quasi-10-day waves
Polar mesospheric clouds
Ice-water content
Wave-mean flow interaction

ABSTRACT

Planetary waves, including quasi-2, -5, -10, −16-day waves, play significant roles in stratospheric dynamics. However, the existing knowledge on quasi-10-day waves (Q10DWs) at high latitudes is limited. This paper investigated the interannual and seasonal variations of Q10DWs with zonal wave numbers varying from the −3 (westward propagation) to 3 (eastward propagation) modes from 2008 to 2022, using temperature data measured by the Microwave Limb Sounder instrument (316−0.001 hPa, corresponding to an altitude of approximately 8–97 km) and temperature/ice water content data measured by the Solar Occultation for Ice Experiment (SOFIE) instrument (10−100 km at latitudes >55°). The findings revealed that the amplitude of Q10DWs in winter was higher than that in other seasons. The amplitude of Q10DWs was observed to substantially decrease with an increase in wavenumber. In addition, the amplitude of stationary Q10DWs in the northern polar region exceeded that in the southern polar region. Moreover, we used observational data from the SOFIE instrument, which simultaneously measures temperature and ice water content (IWC) in the mesosphere, to examine the variations of Q10DWs with respect to the temperature and IWC. Our findings suggest that in the northern polar region, the maximum value of Q10DWs in IWC was occasionally observed earlier than the lowest value of Q10DWs in temperatures.

1. Introduction

Planetary waves (PWs) originate from longitudinal variations in topography and heating; they are driven by the Coriolis force. These waves play vital roles in atmospheric dynamics and ionospheric electrodynamics [1–6]. PWs are generally categorized as free or forced waves. A series of classical normal modes was derived by solving the Laplace tidal equation [7]. Among them, the Rossby

* Corresponding author. State Key Laboratory of Lunar and Planetary Sciences, Macau University of Science and Technology, Taipa, 999078, Macau, People's Republic of China.
** Corresponding author. State Key Laboratory of Lunar and Planetary Sciences, Macau University of Science and Technology, Taipa, 999078, Macau, People's Republic of China.
E-mail addresses: sfu@must.edu.mo (S. Fu), yjiang@must.edu.mo (Y. Jiang).
[1] Contributed equally. Yucheng Su and Boyang Jiao contributed equally to this work.

https://doi.org/10.1016/j.heliyon.2024.e31241
Received 5 January 2024; Received in revised form 13 May 2024; Accepted 13 May 2024
Available online 14 May 2024

normal mode exhibits westward propagation with periods of ~2, 5, 10, and 16 days, commonly called quasi-2-day waves (Q2DWs), quasi-5-day waves (Q5DWs), quasi-10-day waves (Q10DWs), and quasi-16-day waves (Q16DWs), respectively [4,6,8].

These normal modes have been extensively studied over the past few decades, with a particular focus on Q2DWs and Q5DWs [1–6, 9,10]. However, Q10DWs have not attracted considerable attention due to limited observations [8,11,12]. Hirooka [13] studied the Q10DWs in the stratosphere and lower mesosphere using measurements from the Upper Atmosphere Research Satellite/Improved Stratosphere and Mesospheric Sounder (UARS/ISAMS) over 1991–1992. Recently, using temperature measurements from the Thermosphere Ionosphere Mesosphere Energetics Dynamics/Sounding of the Atmosphere using Broadband Emission Radiometry (TIMED/SABER), Forbes and Zhang [8] (hereinafter, FZ15) investigated westward-propagating Q10DWs with a latitudinal wave number (denoted by s) of 1. Their findings revealed a notable alignment with the theoretical expectations of the normal mode, along with a mean period of 9.8 days and a standard deviation of ~0.4 days. FZ15 demonstrated that Q10DWs are weak and strong during summer and winter at middle latitudes, respectively. However, due to the limited TIMED/SABER observations, FZ15 only analyzed the Q10DWs in the temperature within an altitude range of 20–100 km and within latitudes of ±50°. Nevertheless, it is theoretically expected that Q10DWs will be strong at high latitudes (above ±50°), which is their normal mode behavior [8]. Thus, FZ15 postulated that Q10DWs are pronounced at high latitudes, and one of the goals of this study is to investigate this hypothesis through observational analysis. Additionally, the investigation of Q10DW counterparts, particularly in mesospheric clouds, has rarely been explored; thus, it is another goal of this study.

Polar mesospheric clouds (PMCs) comprise a delicate layer of water ice particles that condense near the polar summer mesopause on meteoric smoke particles [14]. Many factors, such as water vapor, temperature, and nucleation nuclei, collectively contribute to PMC formation. The occurrence and abundance of PMCs have been observed to be closely tied to the dynamics and microphysics of the polar summer mesosphere. Thus, PMCs reflect changes in the global temperature and water vapor [14–20]. Kirkwood et al. (2003) [64] observed a strong correlation between the probability of observing PMCs and the combined effects of stationary Q16DWs and Q5DWs at the PMC locations using 40 years of PMC observations. Moreover, von Savigny et al. [21] observed a good agreement in the Q5DWs of PMC occurrence rates and mesopause temperatures based on PMC data obtained using the Scanning Imaging Absorption Spectrometer for Atmospheric CHartographY (SCIAMACHY) instrument with temperatures measured using the Microwave Limb Sounder (MLS). Several reports [4,22–25] further discuss how Q5DWs modulate PMCs. However, to the best of our knowledge, no studies have reported the relation between Q10DWs in mesospheric temperature and Q10DWs in the ice-water content (IWC) of PMCs. To examine the phase shift of the Q10DWs in temperature and PMCs, we investigate the concurrent measurements of temperature and IWC throughout the entire PMC seasons. The other goal of this study is to investigate the climatology of Q10DWs in the polar stratosphere and mesosphere through the Solar Occultation for Ice Experiment (SOFIE) and MLS observations.

The remainder of the paper is arranged as follows. Section 2 describes the observations and method employed to extract PWs. Section 3 presents the global distribution of Q10DWs, their seasonal variations, and interhemispheric asymmetry at high latitudes, along with an analysis of their dependence on height and wavenumber. Section 4 discusses the phase shift of the W1 Q10DWs in temperature and IWC. Finally, Section 5 summarizes the results.

2. Materials and methods

To examine the variations of Q10DWs at high latitudes (above ±50°), we employed temperature measurements obtained using the MLS instruments and temperature/IWC measurements obtained using the SOFIE instruments.

The Aeronomy of Ice in the Mesosphere (AIM) satellite is dedicated to studying PMCs and the chemistry and dynamics of the mesosphere. The AIM/SOFIE instrument is used for solar occultation measurements at 16 wavelengths of 0.292–5.316 μm to determine vertical profiles of temperature, O_3, H_2O, CO_2, CH_4, NO, PMC extinction, and meteoric smoke extinction [16,18,26,27]. This study obtained data using SOFIE (version 1.3), which is available online (sofie.gats-inc.com). During polar summer in the Southern Hemisphere (SH), the temperature accuracy of SOFIE v1.3 was within 2 K compared to that of SABER at altitudes below the mesopause [28]. During polar summer in the Northern Hemisphere (NH), the temperature accuracy of SOFIE v1.3 was within 2 K compared to that of SABER at altitudes below ~ 80 km and up to 4 K warmer than that of SABER at an altitude ranging from ~80 to 90 km. The measurements had a vertical resolution and path length of ~1.8 and ~300 km, respectively, and the observations covered polar latitudes (65°–82° South and North). Russell et al. [27] discussed the accuracy of SOFIE measurements and conducted validations (see also references [16–18,26,28,29]).

The SOFIE v1.3 temperatures within the 10−102 km height range were vertically smoothed over 1 km prior to the extraction of Q10DWs. PMCs were observed during summer, specifically around 30–60 days from the solstice (DFS), within an altitude range of ~80–89 km in the northern polar region (NPR) and southern polar region (SPR) [17]. The temperature and PMCs were simultaneously observed, enabling the accurate determination of the phase shift between them. Q10DWs with zonal wavenumbers ranging from −3 (westward propagation) to 3 (eastward propagation) were obtained using the least squares fitting technique on the space–time series of the obtained temperature profiles. To achieve this, we fit the observational temperature at a time (units in UT day) using the following equation:

$$y(\lambda, t) = A\cos\left(\frac{2\pi}{\mathrm{T}}t - \frac{2\pi}{360}s\lambda - \varphi\right), \tag{1}$$

where λ denotes the longitude in degrees, t is the time in days, and A, T, s, and φ denote the amplitude, period, zonal wavenumber, and phase, respectively. Positive and negative wavenumbers indicate eastward and westward propagations, respectively. Further, we

employed the Monte Carlo method [30] to calculate the confidence level of Q10DWs in every fitting window and obtain amplitudes above 0.5 K that are significant at an 80 % confidence level.

The MLS instrument aboard the Aura spacecraft was used to observe thermal microwave limb emissions [31]. The Aura spacecraft maintained a Sun-synchronous orbit at an altitude of 705 km with an inclination of 98°. It can complete an orbit around the Earth every 100 min and conduct 240 scans per orbit, resulting in ~3500 vertical profiles per day along its suborbital track. MLS measurements encompass geographic latitudes ranging from 82°N to 82°S, providing valuable data on the concentrations of various chemical constituents, as well as temperature and geopotential height. The MLS temperatures (316−0.001 hPa, corresponding to 8−97 km) were obtained by inverting the radiance measurements of O_2 from the 118-GHz and isotopic 234-GHz emission lines. The vertical resolution of the MLS temperature products decreased with altitude (e.g., 4 and 14 km at 30 and 0.001 hPa, respectively) [32].

This study used the MLS v4.2 temperature dataset. The validation of these data and the analysis of temperature and geopotential biases have been compared with other reported observational results [32]. They reported a basis of approximately −1 K in temperatures compared with correlative measurements in the troposphere and stratosphere. Moreover, they observed an additional systematic vertical structure with peak-to-peak variations ranging from 2 to 3 K. Given that this study focused on analyzing perturbations around the mean state, the aforementioned systematic biases were expected to have minimal influence on the study findings. As the AIM/SOFIE and Aura/MLS operate in Sun-synchronous orbits, the extraction of Q10DWs using the MLS was conducted with the same methodology as that used for SOFIE. Previous studies have demonstrated the capability of the MLS to observe traveling and stationary PWs [33–35].

3. Results

3.1. Global Q10DWs in MLS temperatures

MLS temperatures (−82°–82°) were used to examine the latitudinal distribution of Q10DWs, and the results were compared with

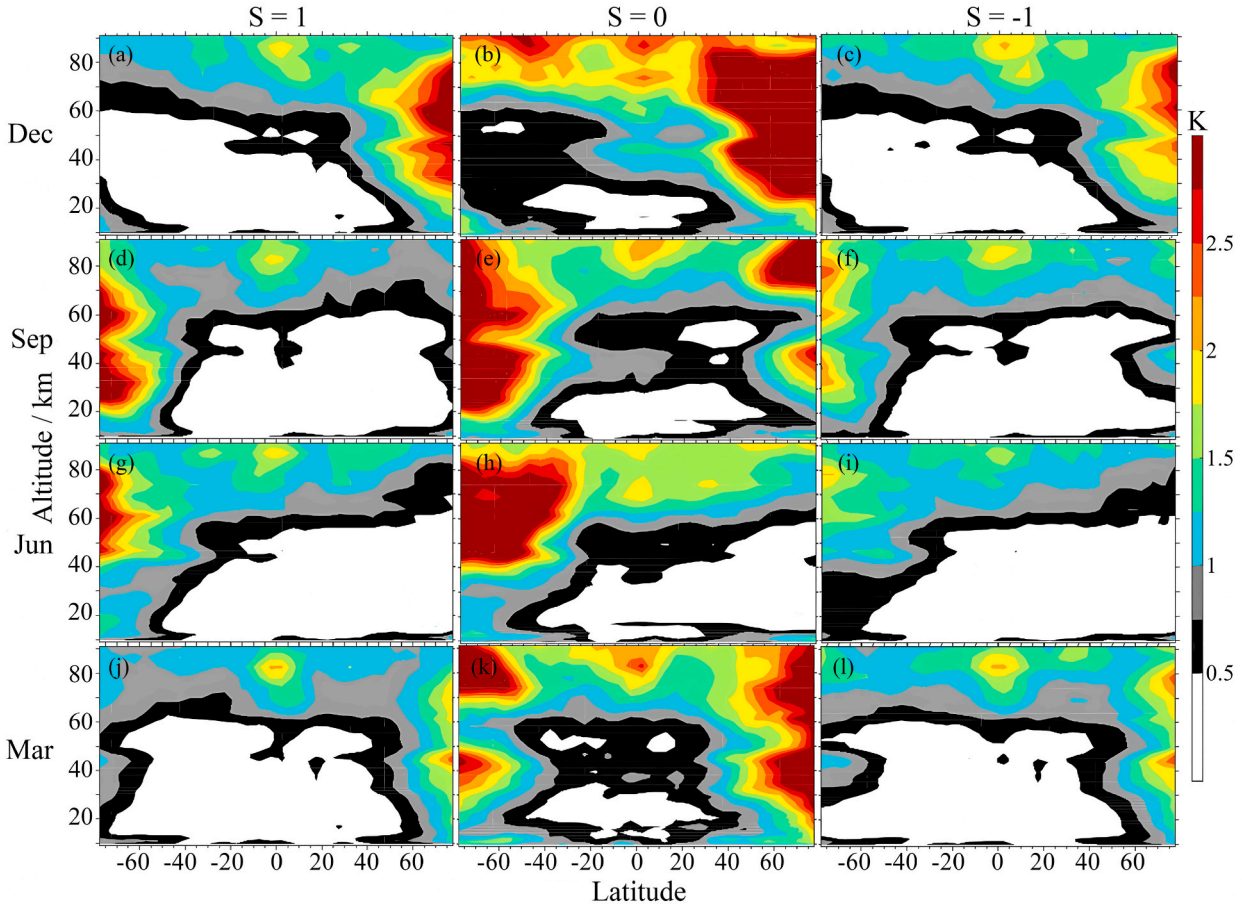

Fig. 1. Latitude versus height structures of Q10DW temperature amplitudes for fitting windows centered on the 15th of December (a–c), September (d–f), June (g–i), March (j–l). The left column (a, d, g, and j), middle column (b, e, h, and k), and right column (c, f, i, and l) correspond to the s = 1, s = 0 (stationary), and s = −1 modes of the Q10DWs, respectively.

those of FZ15 [8]. The data were sorted into latitude bins from −80° to 80° with a width of 5°. There were ~180–250 profiles in each bin per day before quality control. Fig. 1 illustrates the height versus latitude structures of the Q10DW temperature amplitudes. The fitting windows were centered on four specific dates: the 15th of December (Fig. 1a–c), September (Fig. 1d–f), June (Fig. 1g–i), and March (Fig. 1j-l). These dates corresponded to distinct seasonal characteristics, representing winter, autumn, summer, and spring, respectively. We observed that the amplitude of Q10DWs was stronger at high latitudes (>55°) in all months. Furthermore, the larger amplitude of Q10DWs extended from lower (30 km) to higher altitudes (80 km) at high latitudes. Fig. 2 shows the distribution of Q10DW temperature amplitudes as a function of latitude and day of year at altitudes of ~74 km (a-c), ~60 km (d-f), ~45 km (g-i), ~30 km (j-l).

Figs. 1 and 2 indicate that at low altitudes (<60 km), the Q10DWs exhibited peaks at high latitudes in winter. However, above 60 km, the Q10DW amplitude tended to increase over a broader range in latitude and time. The Q10DW was also observed to peak at an altitude above 70 km at mid-latitudes and near the equator. Here, we removed 60 days of the mean nonmigrating tidal components to extract the Q10DWs. However, the disturbing waves of solar tidal modulation and the secondary waves could not be accurately separated. Ground-based observations indicated that the disturbing waves widely existed within an altitude range of 80–100 km [36–40]. The secondary waves [41] generated by the modulation of other PWs with any migrating solar tide also existed within the aforementioned altitude range.

The Q10DW pattern quantified using MLS was similar to those deduced by FZ15 [8] at mid and low latitudes. The results showed that Q10DWs were mostly active during winter and around the equinoxes in both hemispheres and the largest amplitudes were observed in the NH. In FZ15 [8], the Q10DW temperature amplitudes were only observed within the ±50° latitudes using SABER. Compared with the amplitude of Q10DWs at mid to low latitudes, the amplitude of Q10DWs at high latitudes (>55°N/S) was stronger in winter (Fig. 1a-c, 1g-1i, and Fig. 2). In addition, the Q10DW temperature amplitudes with s = 0 and −1 were not weaker than those with s = 1. Thus, it was necessary to study the Q10DW temperature amplitudes at high latitudes, and they were investigated using SOFIE temperatures at high latitudes. Compared with the coarse vertical resolution of MLS temperatures in the mesosphere (14 km at

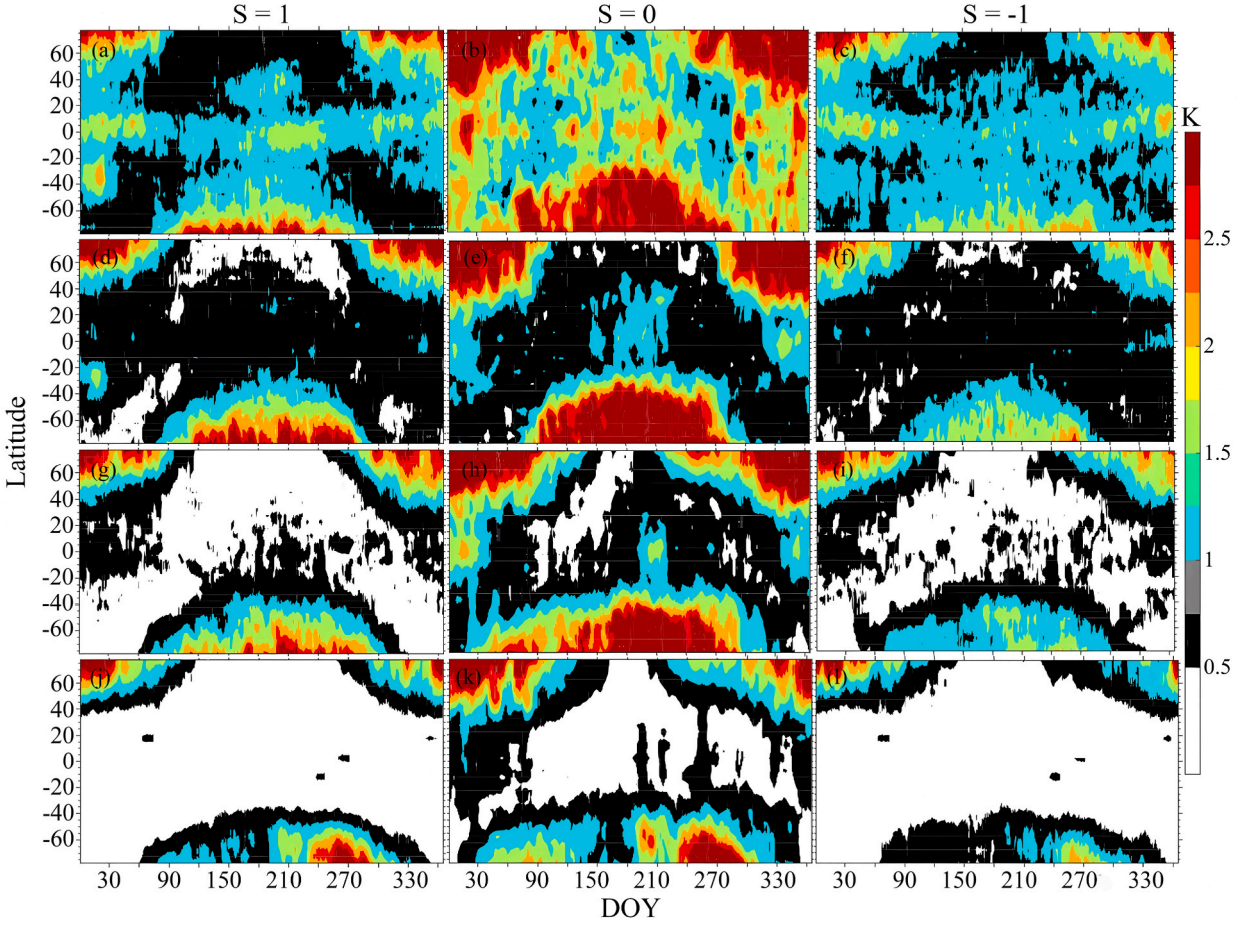

Fig. 2. Latitude versus day-of-year structures of multiyear average (2008–2022) Q10DW temperature amplitudes at altitudes of ~74 km (a–c), ~60 km (d–f), ~45 km (g–i), ~30 km (j–l). The left column (a, d, g, and j), middle column (b, e, h, and k), and right column (c, f, i, and l) correspond to the s = 1, s = 0 (stationary), and s = −1 modes of the Q10DWs, respectively.

0.001 hPa), SOFIE observations had a fine vertical resolution (~1.8 km) that did not change with height.

3.2. Q10DWs at high latitudes in SOFIE temperature

We computed the frequency wavenumber spectrum of PWs using the SOFIE temperature, using a method provided by Salby et al. [7], to ascertain the significant components of the PWs at high latitudes. The PW period is typically in the range of 2–30 days, with a strong seasonal dependence. Thus, in the NH (SH), we obtained the vertical mean spectrum using SOFIE temperatures within an altitude range of 80–90 km (60–80°N/S) from 2008 to 2022. We obtained the normalized frequency–wave number spectrum in each hemisphere (Fig. 3). We observed that, in addition to the Q2DWs (frequency, ~0.5/day) and Q5DWs (frequency, ~0.2/day), the Q10DWs were significant with wavenumbers 1 and −1 in the NPR (Fig. 3b) and SPR (Fig. 3a), respectively. The Q10DWs with s = 0 were not significant in both polar regions.

First, we focused on the evolution of the amplitude of Q10DWs in the time–height contour at high latitudes. Considering that the AIM satellite is on the Sun-synchronous orbit, the relation between longitude (λ_i) and UT (t_i) was simply given by $\lambda_i = 2\pi t_i/(1\ \text{day})$. The Q10DWs were determined through the LS fitting of the residual data for wave periods varying from 8 to 12 days. The amplitude and period of the Q10DWs were the values that yielded the largest amplitude [42].

Fig. 4a and b shows the stationary mode (s = 0) based on the 2008–2022 averages as the contour of the PW in the NPR and SPR, respectively. To conveniently compare the Q10DWs between both hemispheres, we adjusted the date by shifting it forward 6 months in the NPR. The date corresponded to the initial day of every calendar month. The contour lines shown in Fig. 4 represent the mean zonal winds derived from the Modern Era Retrospective Analysis for Research and Applications (MERRA) assimilation model. The amplitude of Q10DWs was larger in winter than in other seasons in both hemispheres. In the NPR, the amplitude of the Q10DWs was the largest in January and increased with an increase in altitude. The amplitudes of Q10DWs exhibited two peaks separately at 35 and 85 km (Fig. 4a). Similarly, the amplitude exhibited two peaks at 30 and 70 km in September in the SPR (Fig. 4b). The amplitude of Q10DWs exceeded 5 K in the lower mesosphere and stratosphere from December to February in the NPR and from July to September in the SPR. The variation was consistent with the annual variation in the zonal westerly wind from 2008 to 2022, as the westerly wind facilitated the upward propagation of PWs [43]. These strong Q10DWs were generated by the baroclinic/barotropic instability in the polar night jet and/or double-jet regions [41,44–46]. However, during summer, the presence of easterly winds impeded the upward propagation of PWs. Consequently, the amplitude of Q10DWs in the polar stratosphere during summer was extremely small, approaching zero.

The propagating modes of the Q10DWs were examined in the NPR and SPR. Fig. 5 shows a multiyear composite analysis of the amplitudes of the Q10DWs of W1–W3 and E1–E3 in the NPR and SPR for 2008–2022 in SOFIE temperature. Fig. 5a–f and 5g–5l indicate the propagating modes of Q10DWs in the NPR and SPR with wavenumbers E1–E3 and W1–W3, respectively. The results showed that the eastward-propagating modes (E1–E3) of the Q10DWs were consistent with the quasi-stationary Q10DWs in both hemispheres. They both exhibited a clear annual variation, with peaks during winter extending from the stratosphere to the lower mesosphere. The amplitude was observed to be dependent on the wavenumber. For example, the Q10DWs with eastward wavenumbers of 1, 2, and 3 (E1–E3) exhibited structures that were very similar to the stationary-mode Q10DWs. In addition, with an increase in the wavenumber, the amplitude of the Q10DWs considerably decreased. The westward and eastward-propagating Q10DWs exhibited the same patterns. In all cases, the annual variation of the Q10DWs was less pronounced above 80 km. Below 80 km, the strongest Q10DWs were in winter, compared with the nearly zero Q10DWs in summer. On the contrary, at 90 km, the amplitude of the Q10DWs in winter, spring, and autumn was larger than that in summer. At 100 km, the Q10DW amplitude exhibited a stronger semiannual variation with peaks in winter and summer.

FZ15 [8] stated that solar or lunar tides cannot be completely removed from the analysis and tides exponentially increase with altitude. Additionally, above 80 km, the dissipation of gravity waves and the subsequent deposition of momentum may excite secondary Q10DWs. This mechanism has been confirmed in the context of stationary PWs with larger amplitudes [43,47–51]. If the Q10DW component of the secondary excitation was sufficiently large, it was comparable to the original Q10DWs, as shown below. We conducted the same analysis using the MLS-based data (as shown in Fig. 6) and arrived at the same conclusion but with smaller

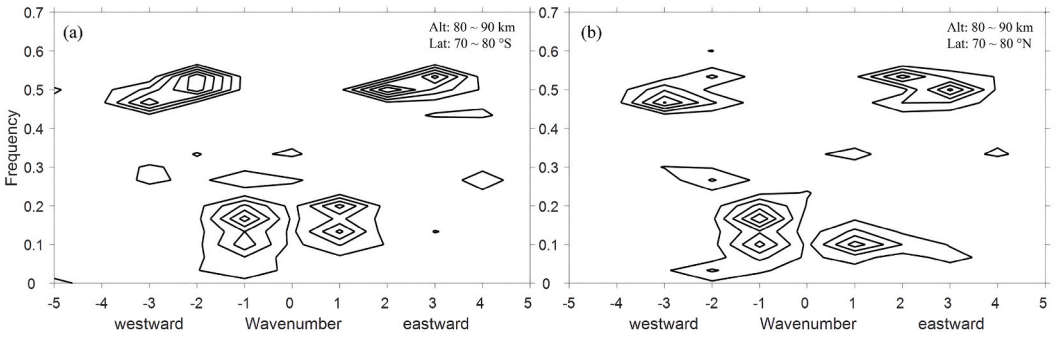

Fig. 3. Normalized mean frequency versus wavenumber spectra of temperature disturbances at high latitudes (70°N/S–80°N/S) in an altitude range of 80–90 km in summer from 2008 to 2022. Panels (a) and (b) show the Southern and Northern Hemispheres, respectively.

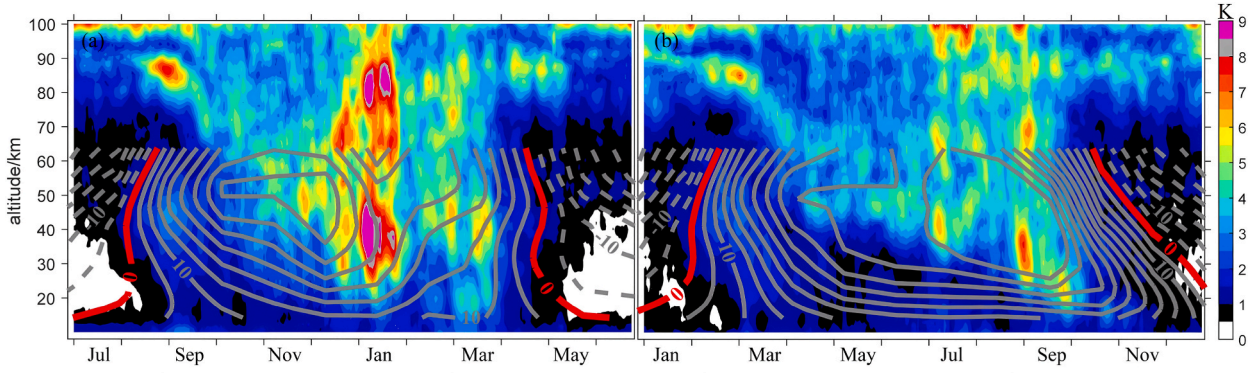

Fig. 4. Composite multiyear analysis of the amplitudes of Q10DWs in temperature with stationary mode (s = 0) in the NPR (a) and SPR (b) extracted from SOFIE data over 2008–2022. The contour lines represent the composite of the mean zonal wind speeds derived from the Modern Era Retrospective Analysis for Research and Applications (MERRA) data in the same period of SOFIE observations. Each contour line has a spacing of 5 m/s. Note that the contour lines with zero values (red line), positive values (solid line), and negative values (dashed line) are the zero, eastward, and westward wind speeds, respectively. To conveniently compare the Q10DWs in the NPR (a) and SPR (b), the date in the NPR was shifted forward by 6 months.

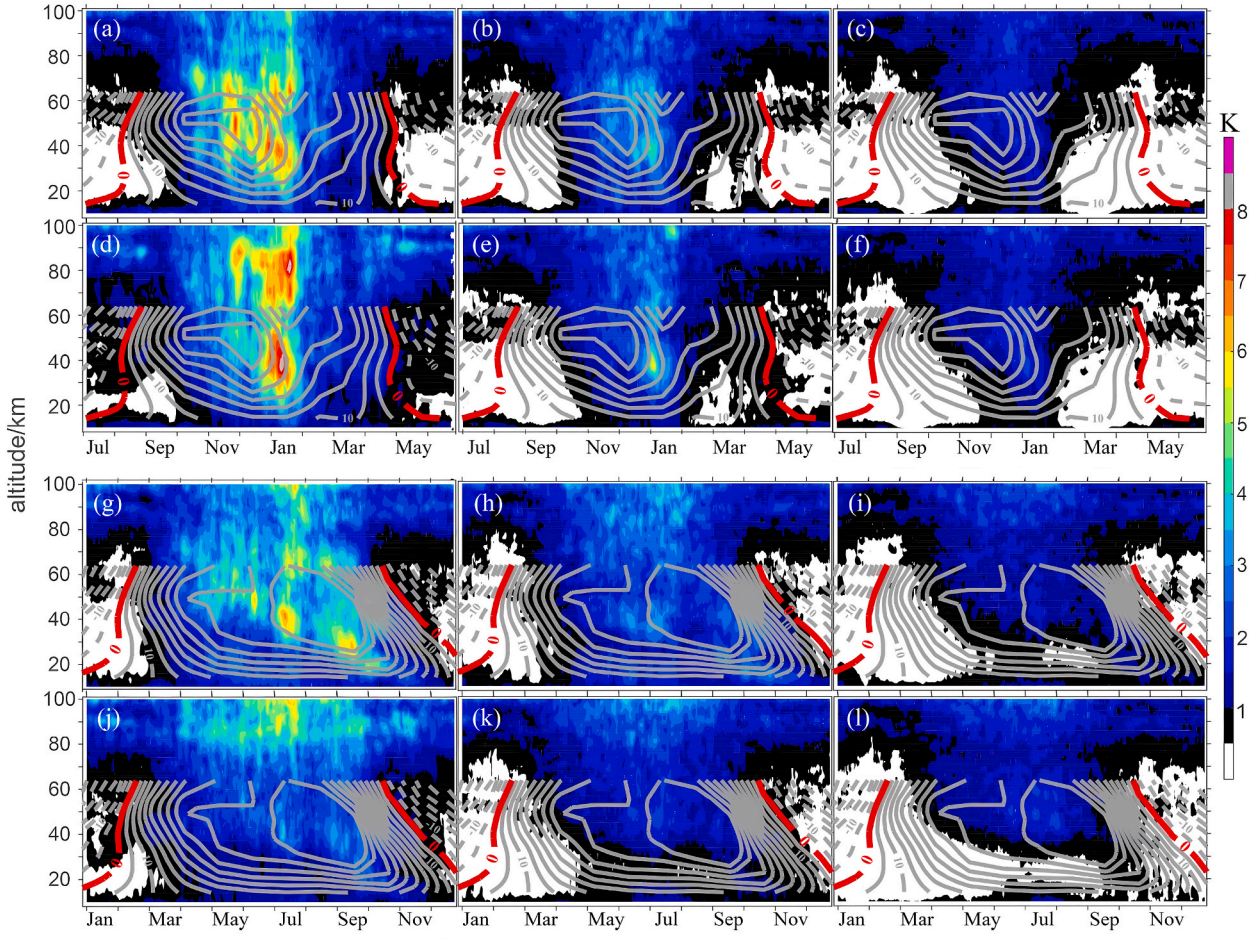

Fig. 5. Composite multiyear analysis of the amplitudes of Q10DWs in temperature in the NPR (a–f) and SPR (g–l) extracted from SOFIE data over 2008–2022. Panels (a) and (g) are for s = 1 mode; panels (b) and (h) are for s = 2 mode; panels (c) and (i) are for s = 3 mode; panels (d) and (j) are for s = −1 mode; panels (e) and (k) are for s = −2 mode; panels (f) and (l) are for s = −3 mode.

amplitudes. A reason for the smaller amplitudes of Q10DWs in the MLS was the coarser MLS vertical resolution.

Next, the evolution of the period corresponding to the maximum amplitude (PCMA) of the Q10DWs was examined based on the time and height. We analyzed the PCMA of the Q10DWs of the stationary and propagating modes (Fig. 7). The period corresponding to the Q10DW amplitudes smaller than 1 K is not shown. Fig. 7a and b indicate the stationary mode of the PCMA of Q10DWs in the NPR/SPR, and Fig. 7c–h and 7i–7n indicate the propagating modes of the PCMA of Q10DWs in the NPR and SPR with wave numbers E1–E3 and W1–W3, respectively. The results showed that in the stationary mode, no significant difference was observed between the numbers of the PCMA of Q10DWs greater than and less than 10 days. Nevertheless, most of the PCMA of Q10DWs less than and greater than 10 days were concentrated above and below 50 km, respectively. In the propagating mode, whether in the NPR/SPR or eastward/westward propagating, the PCMA of the Q10DWs greater than 10 days gradually decreased as the wave number increased. Asymmetries were observed between the NH and SH regarding the PCMA of Q10DWs. The PCMA of the Q10DWs greater than 10 days in the

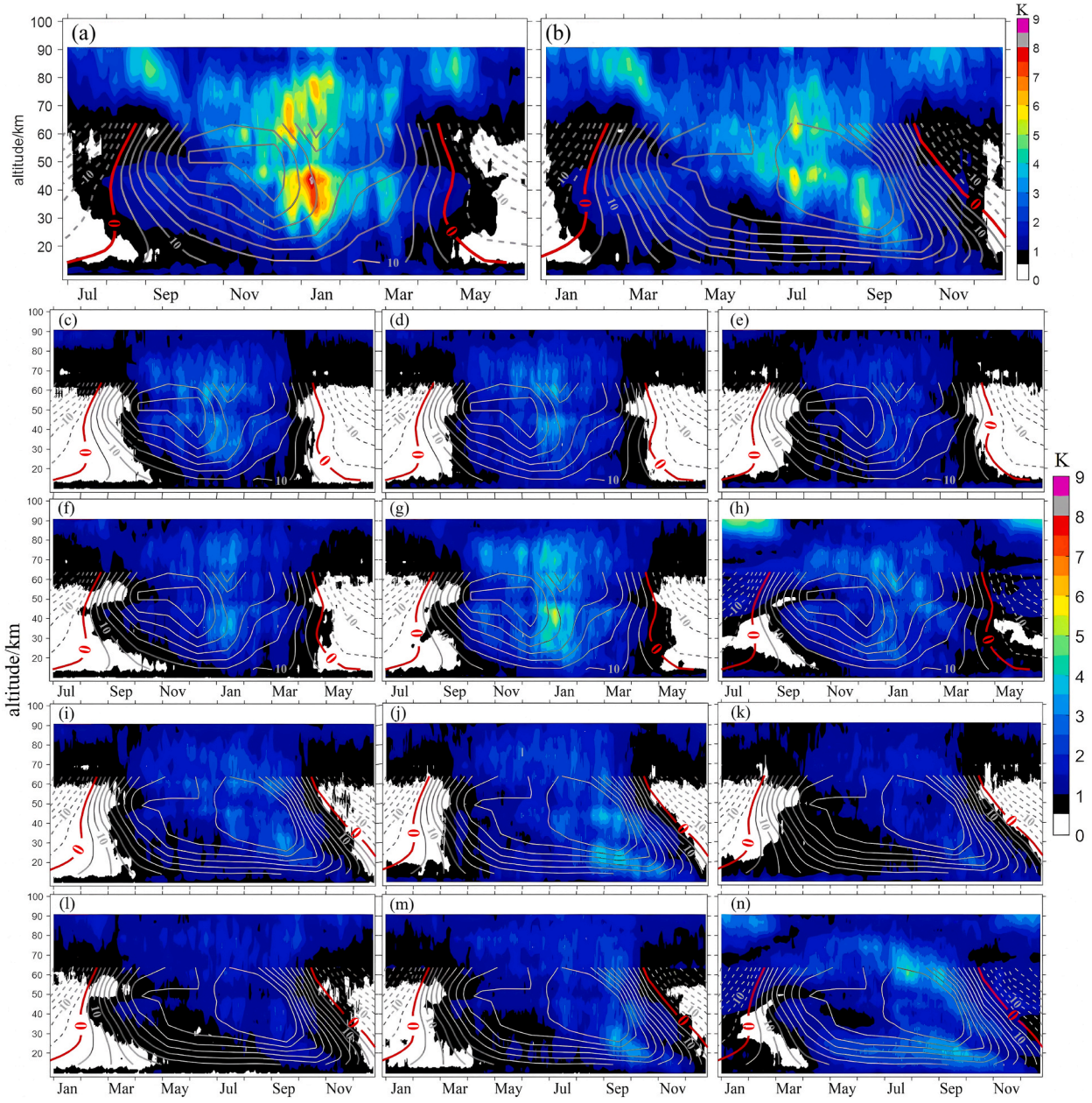

Fig. 6. Composite multiyear analysis of the amplitudes of Q10DWs in temperature in the NPR (panels a and c-h) and SPR (panels b and i-n) extracted from MLS data over 2008–2022. Panels (a) and (b) are stationary mode (s = 0); panels (c) and (i) are for s = 1 mode; panels (d) and (j) are for s = 2 mode; panels (e) and (k) are for s = 3 mode; panels (f) and (l) are for s = −1 mode; panels (g) and (m) are for s = −2 mode; panels (h) and (n) are for s = −3 mode.

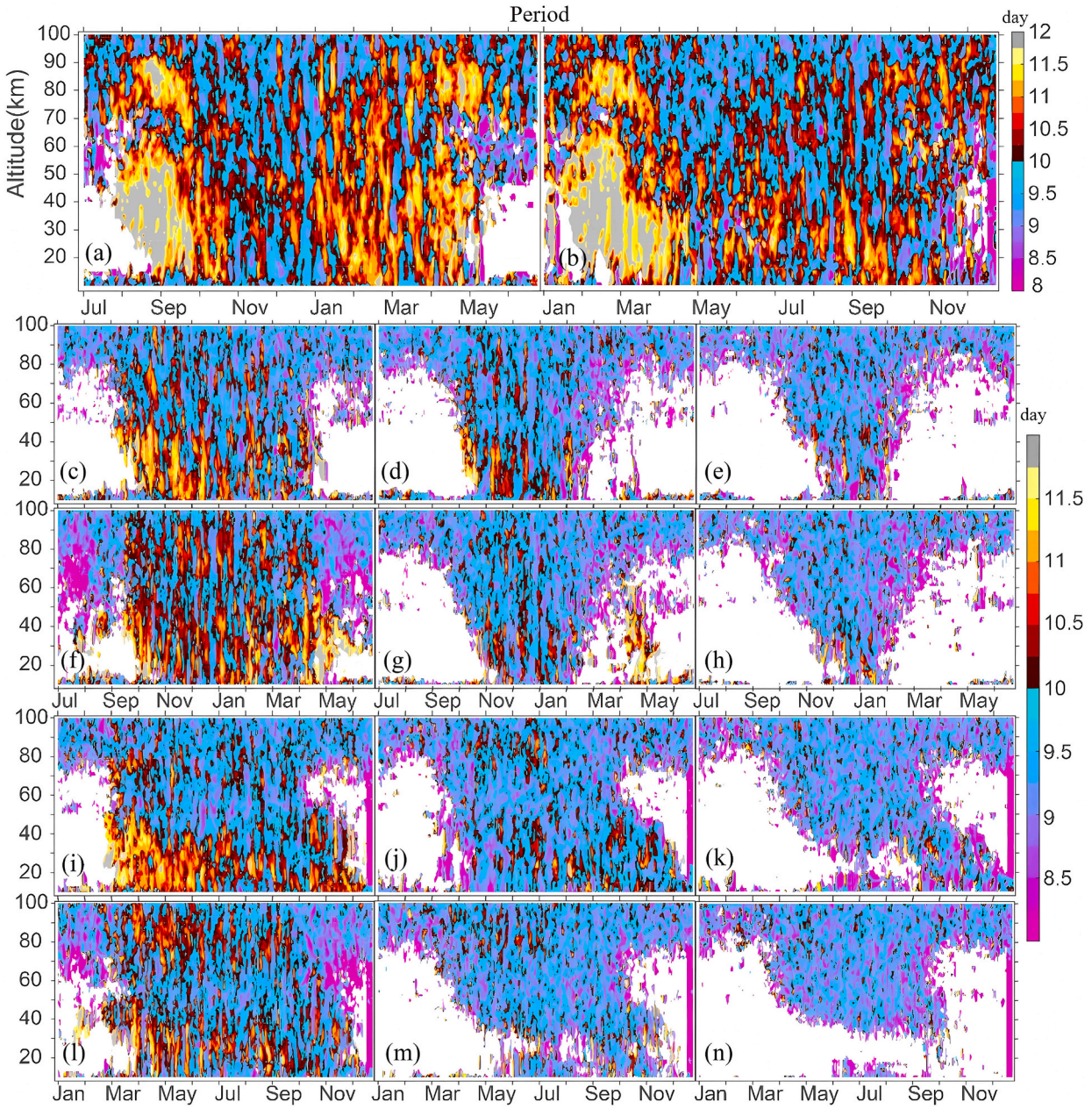

Fig. 7. PCMA of Q10DWs in temperature in the NPR (panels a and c-h) and SPR (panels b and i-n) extracted from MLS data over 2008–2022. Panels (a) and (b) are stationary mode (s = 0); panels (c) and (i) are for s = 1 mode; panels (d) and (j) are for s = 2 mode; panels (e) and (k) are for s = 3 mode; panels (f) and (l) are for s = −1 mode; panels (g) and (m) are for s = −2 mode; panels (h) and (n) are for s = −3 mode.

NPR exceeded that in the SPR at the same time/location. The results of employing the same method to analyze the PCMA of Q10DWs from the MLS data were consistent with the results obtained using SOFIE data. Finally, we analyzed the evolution of the average period of Q10DWs (amplitude >1 K) in time and height. When calculating the average period of Q10DWs with a period between 8 and 12 days, the Q10DW average period was relatively stable around 10 days.

3.3. Q10DWs in temperature and IWC

Herein, we discuss the relation between Q10DWs in temperature and IWC measured simultaneously using the SOFIE instrument in the NPR and SPR. We adopted a band-pass filter with cutoff periods ranging from 8 to 12 days. Fig. 8 illustrates the relation between the Q10DWs in temperature and IWC averaged at an altitude of 81–87 km in the summers of these two hemispheres, during

2008–2022. The *x*-axis label indicates the DFS (number of days from the summer solstices, which fall on 21 June in the NPR and 21 December in the SPR, respectively). The results indicated a complex relation between the Q10DWs in temperature and the IWC anomaly in both the hemispheres. In the NPR, the Q10DWs in temperature and the IWC anomaly typically negatively correlated for −10–5 DFS and 35–60 DFS. The maximum value of the IWC anomaly was observed earlier than the lowest temperatures. Additionally, the Q10DWs in the IWC anomaly began to considerably increase at a DFS of 15, reaching the maximum amplitude at 30 DFS (Fig. 8a). In the SPR, the Q10DWs in the IWC anomaly did not considerably change during summer. The Q10DWs in temperature and the IWC anomaly in the SPR are anticorrelated from −30 to −15 DFS and from 12 to 27 DFS. The maximum value of a 10-day IWC anomaly was observed later than the lowest temperature 2–3 days from the DFS of −17 to the DFS of 12 and the DFS of 27 to the DFS of 65 (Fig. 8b). In the NPR and SPR, the maximum value of the IWC anomaly was observed earlier and later, respectively, than the lowest temperature or was exactly negatively related. In addition, the amplitude of the Q10DWs in the IWC anomaly was extremely volatile in the NPR but remained stable in the SPR.

PMC formation is dependent on many factors, such as temperature, water vapor abundance, and nucleation. PWs can modulate the amount of water vapor through transport. Thus, it is highly possible that the maximum ice water in PMC is not observed during the lowest temperature. In addition, PMC formation can deplete the local water vapor before the temperature decreases to its lowest value [52]. Therefore, even if the temperature decreases, there may not be more ice water. This is why the maximum value of the ice water in the Q5DWs was observed earlier than the lowest temperature recorded in the same wave [21,23,24,53]. Atmospheric fluctuations in various periods can influence atmospheric dynamics, particularly processes such as upwelling and transport, which play crucial roles in regulating the formation of PWC ice particles [54]. In addition, the formation of ice particles can be influenced by other factors, such as nucleation rate, ice core number density, and eddy diffusion [19,25]. Changes in these factors can greatly affect ice formation, consequently influencing the phase difference between Q10DWs in temperature and IWC anomalies. The relation between the Q10DWs in temperature and the IWC anomaly was very different in both hemispheres. Further modeling is required to investigate the relation between the amplitude of the Q10DWs in temperature and the IWC anomaly.

4. Discussion

Based on climatological research, westward-propagating waves with a zonal wavenumber of 1 (s = −1) and eastward-propagating waves with meridional wavenumbers of 1 (s = 1) and 2 (s = 2) have been identified as the predominant propagating waves in Q10DW [55]. As shown in Fig. 3, the amplitude of the Q10DW (s = 0) temperature component should be very close to 0 in both the SH and NH. However, in Figs. 1, 2, 4 and 5, the amplitude of the Q10DW (s = 0) temperature component is considerably larger, with some values exceeding 5 K. The occurrence of the Q10DW (s = 0) temperature component eruption at high latitudes (50–70°N/S) in the winter hemisphere at altitudes of 30–80 km (Figs. 1 and 2) is clearly abnormal. We believe that the Q10DW (s = 0) observed in the middle atmosphere at high latitudes is a mixed wave, including the Q5DW, partial secondary waves, and coupling between and within hemispheres caused by gravity waves. The phenomenon observed in Fig. 1 (s = 0) further supports our hypothesis. Q10DWs can be observed at the upper boundary of the middle atmosphere across all latitudes. Q5DW/Q16DWs are symmetric modes, exhibiting temperature perturbations symmetric about the equator, whereas Q2DW/Q10DWs are antisymmetric modes, with perturbations changing sign at the equator [56]. This suggests that Q10DWs near the equator are expected to be close to 0. However, Fig. 1 shows significant amplitudes of Q10DW (s = 0) observed in equatorial regions above 80-km altitude. This phenomenon is likely caused by shear instability, which during the equinox transition period can considerably amplify PWs above 80 km [57]. In addition, secondary

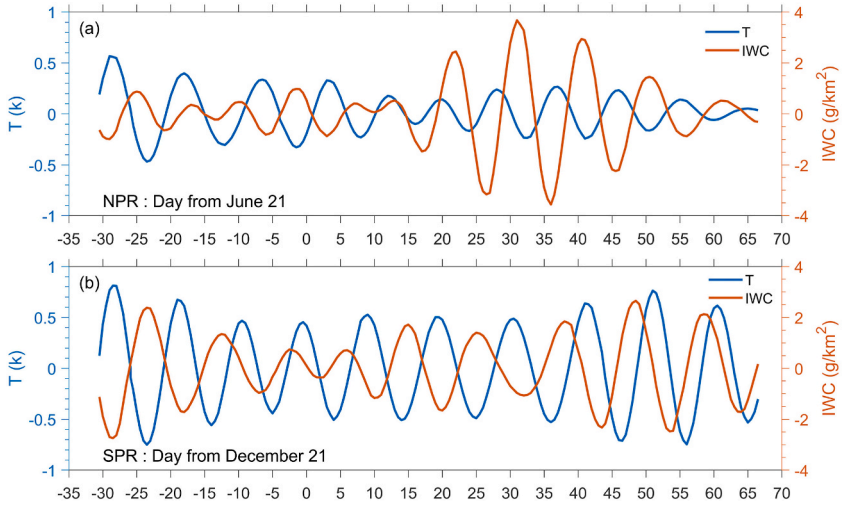

Fig. 8. Composite year analysis of the temporal evolution of Q10DWs in temperature (blue) and IWC (red) averaged between 81 and 87 km altitude during the NPR (a) and SPR (b) summers, extracted from SOFIE data over 2008–2022. The *x*-axis label indicates the number of days from the respective summer solstices (21 June in the NPR and 21 December in the SPR, respectively).

waves are enhanced at this altitude. Fritts et al. [58] demonstrated that secondary waves may result from wave–wave interactions and wave breaking. Secondary waves generated from mountain waves breaking at critical levels below 83 km could propagate to PMC altitudes and account for wave activity over orographic sources. From Figs. 4 and 5 (s = 0), the amplitude of Q10DW primarily peaks in the winter hemisphere (at 30–60 and 70–90 km). However, the peak in the amplitude of Q10DW (s = 1) at 70–90 km disappears, further confirming our hypothesis.

During the winter half-year, the amplitude of Q10DW (s = 1) near the top of the stratosphere at high latitudes is significant. Eastward background winds that are slower than the phase speed of Q10DW (s = 1) hinder its propagation. In addition, thick evanescence regions between 18 and 25 km impede the propagation of s = 1 waves [59]. Therefore, we speculate that the large amplitude of Q10DW (s = 1) at the high-latitude stratospheric top is due to the interaction between locally excited waves and upward propagating waves. In the NH, the Q10DW (s = 1) experiences favorable transmission conditions in the winter troposphere (shear instability) and may propagate upward, ultimately resulting in strong wave activity at the stratospheric top. On the contrary, in the SH, the Q10DW (s = 1) excited at the tropospheric top does not propagate upward because the background winds are not conducive to upward propagation. During the summer half-year, the propagation conditions for the Q10DW (s = −1) are very poor, leading to minimal wave activity during this period. Although the propagation conditions for the Q10DW (s = −1) are favorable in spring and autumn, no Q10DWs (s = −1) are present at the top of the troposphere during these seasons. We speculate that the Q10DW (s = −1) is more active in the troposphere during winter than during the other two seasons. In the summer months, thick evanescence regions around 20 km hinder upward wave propagation in the troposphere and thick evanescence regions above 40 km further impede upward propagation. Therefore, the activity of the Q10DW (s = −1) across the entire altitude range during summer is relatively weak. In high-latitude regions, both the Q10DWs (s = 1 and s = −1) exhibit relatively strong activity, with the Q10DW (s = −1) having better propagation conditions from the troposphere upward than Q10DW (s = 1). The Q10DW (s = −1) excited in the troposphere in the NH can easily propagate upward into the stratosphere and mesosphere. We speculate that the Q10DW (s = 1) in both hemispheres may be excited *in situ* and interact with downward-propagating waves, resulting in intense wave activity. Generally, the seasonal Q10DW variation differs, and its spatial and temporal distributions are primarily determined by wave propagation conditions.

Temperature, water vapor abundance, and nucleation all play a role in PMC formation. In summer, upwelling occurs at high latitudes and the ascending air is adiabatically cooled to temperatures lower than 150 K [60]. In addition to lowering the temperatures, this upward flow transports water vapor to the summer polar mesopause region to remain in the super-saturated altitude range for a longer period so that it can grow larger. Because supersaturation is exponentially dependent on temperature and only linearly dependent on water vapor, clouds are primarily controlled by temperature [18,61]. The 11-year solar cycle, coupling between and within hemispheres caused by gravity waves, and PW activity influence PMC formation seasons by affecting temperature. PMC in SH is more variable and generally darker than that in NH [61]. Further, the relation between PMC and temperature in SH is more complex in the SH than in the NH (Fig. 8). PMC formation in the summer polar regions of the SH is hindered by persistent SH stratospheric polar vortices, which extend until the end of December and continue to influence wave propagation to the middle atmosphere. This influence is stronger in the SH than in the NH because the breakdown of polar vortices occurs much later in the SH. Walterscheid [62] and Liu [63] reported that atmospheric gravity wave breaking in a low thermosphere can produce a downward heat flux, which cools the mesopause region and heats the region immediately below. There is a highly significant correlation between IWC and atmospheric perturbations induced by Q5DW, Q16DW, and stationary PWs [64]. In theory, Q10DWs do not directly influence PMC variations because Q10DWs are predominantly present in the winter hemisphere, with very weak activity in the summer hemisphere where PMCs occur only at high latitudes. However, in Fig. 8, we still observe a complex relation between the temperature and IWC of the Q10DWs. This complexity arises because the filtered Q10DW primarily includes Q5DW, partial secondary waves, and coupling between and within the hemispheres caused by gravity waves. This leads to an intriguing conclusion: even when the filtered Q10DW is considered solely as a climatological diagnostic factor, without considering its complex climate dynamics, it can still reveal certain PMC variations.

5. Conclusion

Theoretically, in the middle and upper atmospheric levels, the amplitude of Q10DWs is higher at high latitudes than at the low and middle latitudes. However, studies on the confirmation of this theory are limited because of the scarcity of satellite observations. The counterparts of Q10DWs have rarely been studied, particularly in terms of PWC. The time–height and wavenumber dependence of Q10DWs at high latitudes is presented using AIM/SOFIE and Aura/MLS temperature measurements over 2008–2022. Moreover, the relations between the Q10DWs in temperature and the corresponding PMC IWCs were explored. The overall conclusions are as follows.

The amplitude of the Q10DWs decreased with an increase in the zonal wavenumber and was larger at high latitudes (>55°) than at lower latitudes in both hemispheres in all months. At lower altitudes (<60 km), the largest amplitude was only observed at high latitudes in winter. As the height increased, the amplitude extended to a wider latitude range and covered a longer-lasting time. The amplitude was larger in winter than in other seasons at high latitudes in both hemispheres. In the NPR/SPR, the amplitude of the Q10DWs was the largest in January/September. With an increase in altitude, the amplitude appeared to exhibit a strong (35/30 km)–weak (60/55 km)–strong (85/70 km) pattern. In addition, with an increase in the wavenumber, the amplitude of the Q10DWs considerably decreased. The westward and eastward-propagating Q10DW exhibited similar patterns. The seasonal variation of Q10DW varied, and its spatial and temporal distribution was primarily influenced by wave propagation conditions.

The amplitude of the Q10DWs exhibited an asymmetry between both hemispheres, which was dependent on height and zonal wavenumbers. In the stationary mode, the amplitude in the NPR was larger than that in the SPR. As the wavenumber increased, the amplitudes in both hemispheres decreased, and the decrease in the amplitude in the SPR was more significant than that in the NPR.

Most of the PCMAs of the Q10DWs less and greater than 10 days were concentrated above and below 50 km, respectively, in the stationary mode. In the propagating mode, the PCMA of the Q10DWs greater than 10 decreased as the wave number increased whether in the NPR/SPR or eastward/westward-propagating mode. When the wave number was −3/3, practically all the PCMAs were less than 10.

The maximum IWC value was observed earlier than the lowest temperature (from the DFS of −27 to the DFS of −10) or was exactly negatively related (from the DFS of −10 to the DFS of 5 and from the DFS of 35 to the DFS of 60) in the NPR. On the contrary, the maximum IWC value was observed later than the lowest temperature (from the DFS of −17 to the DFS of 12 and from the DFS of 27 to the DFS of 65) or was exactly negatively related (from the DFS of −30 to the DFS of −15 and from the DFS of 12 to the DFS of 27), in the SPR. Moreover, the amplitude of the Q10DWs in IWC varied more than that in the NPR than in the SPR. In theory, Q10DWs in the middle atmosphere cannot explain variations in PMC. However, using Q10DWs as a diagnostic indicator for PMCs might be a promising approach. This is because temperature Q10DWs not only incorporate the influences of the Q5DW, secondary waves, and tidal waves that affect PMCs but are also closely related to the 11-year solar cycle that impacts PMCs.

Funding statement

This work was supported by the National Natural Science Foundation of China [Grant No. 12250012], the Science and Technology Development Fund of Macau [Grant no. 0064/2023/ITP2], the Faculty Research Grants of the Macau University of Science and Technology [Grant No. FRG-23-032-SSI], and the Specialized Research Fund for State Key Laboratories.

Data availability statement

All data used in this work are publicly available. MERRA-2 simulations (version 5.12.4) are available from NASA's Data and Information Services Center website (https://disc.gsfc.nasa.gov/datasets/M2I6NVA-NA_5.12.4/summary). The PMC data obtained from AIM/SOFIE are available from the SOFIE website (http://sofie.gats-inc.com/sofie/index.php). The MLS data can be downloaded from: https://avdc.gsfc.nasa.gov/pub/data/satellite/Aura/MLS/V05/L2GP/. The MERRA-2 data can be downloaded from: https://disc.gsfc.nasa.gov/datasets/.

CRediT authorship contribution statement

Yucheng Su: Writing – original draft, Visualization, Software, Methodology, Formal analysis, Data curation. **Boyang Jiao:** Writing – original draft, Visualization, Validation, Software, Methodology, Investigation, Formal analysis, Data curation. **Shuai Fu:** Writing – review & editing, Supervision, Funding acquisition, Data curation, Conceptualization. **Yi Jiang:** Writing – review & editing, Validation, Funding acquisition.

Declaration of competing interest

The authors declare that they have no known competing financial interests or personal relationships that could have appeared to influence the work reported in this paper.

Acknowledgements

The authors would like to express their gratitude to Profs. Jia Yue, Xiao Liu, Mark Hervig, and James Russell for their valuable discussions and suggestions.

References

[1] D. Altadill, E.M. Apostolov, Time and scale size of planetary wave signatures in the ionospheric F region: role of the geomagnetic activity and mesosphere/lower thermosphere winds, J. Geophys. Res.: Space Phys. 108 (2003), https://doi.org/10.1029/2003JA010015.
[2] G. Jiang, J. Xu, J. Xiong, et al., A case study of the mesospheric 6.5-day wave observed by radar systems, J. Geophys. Res. Atmos. 113 (2008), https://doi.org/10.1029/2008JD009907.
[3] H.-L. Liu, W. Wang, A.D. Richmond, et al., Ionospheric variability due to planetary waves and tides for solar minimum conditions, J. Geophys. Res.: Space Phys. 115 (2010), https://doi.org/10.1029/2009JA015188.
[4] X. Liu, J. Yue, J. Xu, et al., Five-day waves in polar stratosphere and mesosphere temperature and mesospheric ice water measured by SOFIE/AIM, J. Geophys. Res. Atmos. 120 (2015) 3872–3887, https://doi.org/10.1002/2015JD023119.
[5] A.I. Pogoreltsev, A.A. Vlasov, K. Fröhlich, et al., Planetary waves in coupling the lower and upper atmosphere, J. Atmos. Sol. Terr. Phys. 69 (2007) 2083–2101, https://doi.org/10.1016/j.jastp.2007.05.014.
[6] J. Yue, W. Wang, A.D. Richmond, et al., Quasi-two-day wave coupling of the mesosphere and lower thermosphere-ionosphere in the TIME-GCM: two-day oscillations in the ionosphere, J. Geophys. Res.: Space Phys. 117 (2012), https://doi.org/10.1029/2012JA017815.
[7] M.L. Salby, Sampling theory for asynoptic satellite observations. Part II: fast fourier synoptic mapping, J. Atmos. Sci. 39 (1982) 2601–2614, https://doi.org/10.1175/1520-0469(1982)039<2601:STFASO>2.0.CO;2.
[8] J.M. Forbes, X. Zhang, Quasi-10-day wave in the atmosphere, J. Geophys. Res. Atmos. 120 (11) (2015), https://doi.org/10.1002/2015JD023327, 079-11,89.
[9] D. Pancheva, P. Mukhtarov, D.E. Siskind, The quasi-6-day waves in NOGAPS-ALPHA forecast model and their climatology in MLS/Aura measurements (2005–2014), J. Atmos. Sol. Terr. Phys. 181 (2018) 19–37, https://doi.org/10.1016/j.jastp.2018.10.008.
[10] D. Pancheva, P. Mukhtarov, D.E. Siskind, et al., Global distribution and variability of quasi 2 day waves based on the NOGAPS-ALPHA reanalysis model, J. Geophys. Res.: Space Phys. 121 (11) (2016), https://doi.org/10.1002/2016JA023381, 422-11,49.

[11] M. He, J.L. Chau, J.M. Forbes, et al., Quasi-10-Day wave and semidiurnal tide nonlinear interactions during the southern hemispheric SSW 2019 observed in the northern hemispheric mesosphere, Geophys. Res. Lett. 47 (2020) e2020GL091453, https://doi.org/10.1029/2020GL091453.
[12] Y. Qin, S.-Y. Gu, X. Dou, A new mechanism for the generation of quasi-6-day and quasi-10-day waves during the 2019 antarctic sudden stratospheric warming, J. Geophys. Res. Atmos. 126 (2021) e2021JD035568, https://doi.org/10.1029/2021JD035568.
[13] T. Hirooka, Normal mode Rossby waves as revealed by UARS/ISAMS observations, J. Atmos. Sci. 57 (2000) 1277–1285, https://doi.org/10.1175/1520-0469(2000)057<1277:NMRWAR>2.0.CO;2.
[14] M.E. Hervig, L.E. Deaver, C.G. Bardeen, et al., The content and composition of meteoric smoke in mesospheric ice particles from SOFIE observations, J. Atmos. Sol. Terr. Phys. 84–85 (2012) 1–6, https://doi.org/10.1016/j.jastp.2012.04.005.
[15] M. Hervig, R.E. Thompson, M. McHugh, et al., First confirmation that water ice is the primary component of polar mesospheric clouds, Geophys. Res. Lett. 28 (2001) 971–974, https://doi.org/10.1029/2000GL012104.
[16] M.E. Hervig, L.L. Gordley, M.H. Stevens, et al., Interpretation of SOFIE PMC measurements: cloud identification and derivation of mass density, particle shape, and particle size, J. Atmos. Sol. Terr. Phys. 71 (2009) 316–330, https://doi.org/10.1016/j.jastp.2008.07.009.
[17] M.E. Hervig, D.E. Siskind, M.H. Stevens, et al., Inter-hemispheric comparison of PMCs and their environment from SOFIE observations, J. Atmos. Sol. Terr. Phys. 104 (2013) 285–298, https://doi.org/10.1016/j.jastp.2012.10.013.
[18] M.E. Hervig, M.H. Stevens, L.L. Gordley, et al., Relationships between polar mesospheric clouds, temperature, and water vapor from Solar Occultation for Ice Experiment (SOFIE) observations, J. Geophys. Res. Atmos. 114 (2009), https://doi.org/10.1029/2009JD012302.
[19] M. Rapp, G.E. Thomas, Modeling the microphysics of mesospheric ice particles: assessment of current capabilities and basic sensitivities, J. Atmos. Sol. Terr. Phys. 68 (2006) 715–744, https://doi.org/10.1016/j.jastp.2005.10.015.
[20] G.E. Thomas, Is the polar mesosphere the miner's canary of global change? Adv. Space Res. 18 (1996) 149–158, https://doi.org/10.1016/0273-1177(95)00855-9.
[21] C. von Savigny, C. Robert, H. Bovensmann, et al., Satellite observations of the quasi 5-day wave in noctilucent clouds and mesopause temperatures, Geophys. Res. Lett. 34 (2007), https://doi.org/10.1029/2007GL030987.
[22] S. Benze, C.E. Randall, M.T. DeLand, et al., Comparison of polar mesospheric cloud measurements from the Cloud Imaging and Particle Size experiment and the solar backscatter ultraviolet instrument in 2007, J. Atmos. Sol. Terr. Phys. 71 (2009) 365–372, https://doi.org/10.1016/j.jastp.2008.07.014.
[23] A.W. Merkel, R.R. Garcia, S.M. Bailey, et al., Observational studies of planetary waves in PMCs and mesospheric temperature measured by SNOE and SABER, J. Geophys. Res. Atmos. 113 (2008), https://doi.org/10.1029/2007JD009396.
[24] A.W. Merkel, D.W. Rusch, S.E. Palo, et al., Mesospheric planetary wave effects on global PMC variability inferred from AIM–CIPS and TIMED–SABER for the northern summer 2007 PMC season, J. Atmos. Sol. Terr. Phys. 71 (2009) 381–391, https://doi.org/10.1016/j.jastp.2008.12.001.
[25] K. Nielsen, D.E. Siskind, S.D. Eckermann, et al., Seasonal variation of the quasi 5 day planetary wave: causes and consequences for polar mesospheric cloud variability in 2007, J. Geophys. Res. Atmos. 115 (2010), https://doi.org/10.1029/2009JD012676.
[26] L.L. Gordley, M.E. Hervig, C. Fish, et al., The solar occultation for ice experiment, J. Atmos. Sol. Terr. Phys. 71 (2009) 300–315, https://doi.org/10.1016/j.jastp.2008.07.012.
[27] J.M. Russell, S.M. Bailey, L.L. Gordley, et al., The Aeronomy of Ice in the Mesosphere (AIM) mission: overview and early science results, J. Atmos. Sol. Terr. Phys. 71 (2009) 289–299, https://doi.org/10.1016/j.jastp.2008.08.011.
[28] M.H. Stevens, L.E. Deaver, M.E. Hervig, et al., Validation of upper mesospheric and lower thermospheric temperatures measured by the Solar Occultation for Ice Experiment, J. Geophys. Res. Atmos. 117 (2012), https://doi.org/10.1029/2012JD017689.
[29] B.T. Marshall, L.E. Deaver, R.E. Thompson, et al., Retrieval of temperature and pressure using broadband solar occultation: SOFIE approach and results, Atmos. Meas. Tech. 4 (2011) 893–907, https://doi.org/10.5194/amt-4-893-2011.
[30] E. Pardo-Igúzquiza, F.J. Rodríguez-Tovar, Spectral and cross-spectral analysis of uneven time series with the smoothed Lomb–Scargle periodogram and Monte Carlo evaluation of statistical significance, Comput. Geosci. 49 (2012) 207–216, https://doi.org/10.1016/j.cageo.2012.06.018.
[31] J.W. Waters, L. Froidevaux, R.S. Harwood, et al., The Earth observing system microwave limb sounder (EOS MLS) on the aura Satellite, IEEE Trans. Geosci. Rem. Sens. 44 (2006) 1075–1092, https://doi.org/10.1109/TGRS.2006.873771.
[32] M.J. Schwartz, A. Lambert, G.L. Manney, et al., Validation of the aura microwave limb sounder temperature and geopotential height measurements, J. Geophys. Res. Atmos. 113 (2008), https://doi.org/10.1029/2007JD008783.
[33] A.J.G. Baumgaertner, A.J. McDonald, R.E. Hibbins, et al., Short-period planetary waves in the Antarctic middle atmosphere, J. Atmos. Sol. Terr. Phys. 70 (2008) 1336–1350, https://doi.org/10.1016/j.jastp.2008.04.007.
[34] V. Limpasuvan, D.L. Hartmann, D.W.J. Thompson, et al., Stratosphere-troposphere evolution during polar vortex intensification, J. Geophys. Res. Atmos. 110 (2005), https://doi.org/10.1029/2005JD006302.
[35] V. Limpasuvan, D.L. Wu, Anomalous two-day wave behavior during the 2006 austral summer, Geophys. Res. Lett. 36 (2009), https://doi.org/10.1029/2008GL036387.
[36] J.M. Forbes, Tidal and Planetary Waves, Book, Tidal and Planetary Waves, 1995.
[37] D. Pancheva, N. Mitchell, H. Middleton, et al., Variability of the semidiurnal tide due to fluctuations in solar activity and total ozone, J. Atmos. Sol. Terr. Phys. 65 (2003) 1–19, https://doi.org/10.1016/S1364-6826(02)00084-6.
[38] D. Pancheva, P. Mukhtarov, Wavelet analysis on transient behaviour of tidal amplitude fluctuations observed by meteor radar in the lower thermosphere above Bulgaria, Ann. Geophys. 18 (2000) 316–331, https://doi.org/10.1007/s00585-000-0316-3.
[39] D. Pancheva, P. Mukhtarov, N.J. Mitchell, et al., A comparative study of winds and tidal variability in the mesosphere/lower-thermosphere region over Bulgaria and the UK, Ann. Geophys. 18 (2000) 1304–1315, https://doi.org/10.1007/s00585-000-1304-3.
[40] D.V. Pancheva, N.J. Mitchell, Planetary waves and variability of the semidiurnal tide in the mesosphere and lower thermosphere over Esrange (68°N, 21°E) during winter, J. Geophys. Res.: Space Phys. 109 (2004), https://doi.org/10.1029/2004JA010433.
[41] H. Teitelbaum, F. Vial, On tidal variability induced by nonlinear interaction with planetary waves, J. Geophys. Res.: Space Phys. 96 (1991) 14169–14178, https://doi.org/10.1029/91JA01019.
[42] V.M. Tunbridge, D.J. Sandford, N.J. Mitchell, Zonal wave numbers of the summertime 2 day planetary wave observed in the mesosphere by EOS Aura Microwave Limb Sounder, J. Geophys. Res. Atmos. 116 (2011), https://doi.org/10.1029/2010JD014567.
[43] A.K. Smith, Longitudinal variations in mesospheric winds: evidence for gravity wave filtering by planetary waves, J. Atmos. Sci. 53 (1996) 1156–1173, https://doi.org/10.1175/1520-0469(1996)053<1156:LVIMWE>2.0.CO;2.
[44] R.R. Garcia, R.S. Lieberman, J.M. Russell, et al., Large-Scale waves in the mesosphere and lower thermosphere observed by SABER, J. Atmos. Sci. 62 (2005) 4384–4399.
[45] X. Lu, X. Chu, T. Fuller-Rowell, et al., Eastward propagating planetary waves with periods of 1–5 days in the winter Antarctic stratosphere as revealed by MERRA and lidar, J. Geophys. Res. Atmos. 118 (2013) 9565–9578, https://doi.org/10.1002/jgrd.50717.
[46] S.E. Palo, J.M. Forbes, X. Zhang, et al., Planetary wave coupling from the stratosphere to the thermosphere during the 2002 Southern Hemisphere pre-stratwarm period, Geophys. Res. Lett. 32 (2005), https://doi.org/10.1029/2005GL024298.
[47] J.R. Holton, The generation of mesospheric planetary waves by zonally asymmetric gravity wave breaking, J. Atmos. Sci. 41 (1984) 3427–3430.
[48] C. McLandress, N.A. McFarlane, Interactions between orographic gravity wave drag and forced stationary planetary waves in the winter northern hemisphere middle atmosphere, J. Atmos. Sci. 50 (1993) 1966–1990, https://doi.org/10.1175/1520-0469(1993)050<1966:IBOGWD>2.0.CO;2.
[49] S. Miyahara, Suppression of stationary planetary waves by internal gravity waves in the mesosphere, J. Atmos. Sci. 42 (1984) 100–112.
[50] M.R. Schoeberl, D.F. Strobel, Nonzonal gravity wave breaking in the winter mesosphere, Dynamics of the Middle Atmosphere. (1984) 45–64.
[51] A.K. Smith, Stationary planetary waves in upper mesospheric winds, J. Atmos. Sci. 54 (1997) 2129–2145, https://doi.org/10.1175/1520-0469(1997)054<2129:SPWIUM>2.0.CO;2.

[52] M.E. Hervig, D.E. Siskind, S.M. Bailey, et al., The influence of PMCs on water vapor and drivers behind PMC variability from SOFIE observations, J. Atmos. Sol. Terr. Phys. 132 (2015) 124–134, https://doi.org/10.1016/j.jastp.2015.07.010.
[53] A.W. Merkel, G.E. Thomas, S.E. Palo, et al., Observations of the 5-day planetary wave in PMC measurements from the student nitric oxide explorer satellite, Geophys. Res. Lett. 30 (2003), https://doi.org/10.1029/2002GL016524.
[54] E.J. Jensen, G.E. Thomas, Numerical simulations of the effects of gravity waves on noctilucent clouds, J. Geophys. Res. Atmos. 99 (1994) 3421–3430, https://doi.org/10.1029/93JD01736.
[55] C. Huang, W. Li, S. Zhang, et al., Investigation of dominant traveling 10-day wave components using long-term MERRA-2 database, Earth Planets Space 73 (2021) 85, https://doi.org/10.1186/s40623-021-01410-7.
[56] Y. Yamazaki, Y. Miyoshi, Ionospheric signatures of secondary waves from quasi-6-day wave and tide interactions, J. Geophys. Res.: Space Phys. 126 (2021) e2020JA028360, https://doi.org/10.1029/2020JA028360.
[57] R.S. Lieberman, D.M. Riggin, S.J. Franke, et al., The 6.5-day wave in the mesosphere and lower thermosphere: evidence for baroclinic/barotropic instability, J. Geophys. Res. Atmos. 108 (2003), https://doi.org/10.1029/2002JD003349.
[58] D.C. Fritts, L. Wang, J. Werne, Gravity wave–fine structure interactions: a reservoir of small-scale and large-scale turbulence energy, Geophys. Res. Lett. 36 (2009), https://doi.org/10.1029/2009GL039501.
[59] Y. Fan, C.M. Huang, S.D. Zhang, et al., Long-Term study of quasi-16-day waves based on ERA5 reanalysis data and EOS MLS observations from 2005 to 2020, J. Geophys. Res.: Space Phys. 127 (2022) e2021JA030030, https://doi.org/10.1029/2021JA030030.
[60] F.-J. Lübken, Thermal structure of the Arctic summer mesosphere, J. Geophys. Res. Atmos. 104 (1999) 9135–9149, https://doi.org/10.1029/1999JD900076.
[61] B. Karlsson, C.E. Randall, T.G. Shepherd, et al., On the seasonal onset of polar mesospheric clouds and the breakdown of the stratospheric polar vortex in the Southern Hemisphere, J. Geophys. Res. Atmos. 116 (2011), https://doi.org/10.1029/2011JD015989.
[62] R.L. Walterscheid, Inertio-gravity wave induced accelerations of mean flow having an imposed periodic component: implications for tidal observations in the meteor region, J. Geophys. Res.: Oceans 86 (1981) 9698–9706, https://doi.org/10.1029/JC086iC10p09698.
[63] H.-L. Liu, Temperature changes due to gravity wave saturation, J. Geophys. Res. Atmos. 105 (2000) 12329–12336, https://doi.org/10.1029/2000JD900054.
[64] S. Kirkwood, K. Stebel, Influence of planetary waves on noctilucent cloud occurrence over NW Europe, J. Geophys. Res. Atmos. 108 (2003), https://doi.org/10.1029/2002JD002356.